AIAA JOURNAL
Vol. 45, No. 10, October 2007

Aeroacoustic Computations Using a High-Order Shock-Capturing Scheme

Virginie Daru* and Xavier Gloerfelt†
Ecole Nationale Supérieure d'Arts et Métiers, 75013 Paris, France

DOI: 10.2514/1.28518

For aeroacoustic computations in the supersonic regime, it is necessary to use a numerical scheme that can represent shock waves without generating spurious numerical oscillations. The centered schemes that are usually used with success in the subsonic case, combined with a selective filtering, will generally oscillate in the presence of discontinuities. A new class of shock-capturing schemes, the one-step monotonicity-preserving schemes, combine the high accuracy and the nonoscillating property. It is thus a good candidate for supersonic aeroacoustic applications. The good spectral properties of these schemes are illustrated in the scalar linear case. Results of aeroacoustic test problems for the Euler and Navier–Stokes equations are compared with a dispersion-relation-preserving scheme. The application to a supersonic cavity flow, which induces a complex pattern of moving shocks, shows that the one-step monotonicity-preserving schemes capture the moving discontinuities without spurious oscillations and preserve a high accuracy at the same time.

Nomenclature

a	=	convection speed
a_l	=	coefficients of the dispersion-relation-preserving finite difference scheme
c_∞	=	ambient sound speed
D	=	cavity depth
D^f	=	transfer function of the dispersion-relation-preserving filter
d_l	=	coefficients of the dispersion-relation-preserving filter
$d_{j+1/2}$	=	curvature term
$F^p_{j+1/2}$	=	numerical flux
f	=	frequency
G	=	amplification factor
J_m	=	Bessel function of the first kind and order m
k	=	wave number
$k^\star$	=	effective wave number of a scheme
L	=	cavity length
l	=	half-distance between the vortices (corotating-vortex test case)
M	=	Mach number
M_r	=	rotation Mach number
n_a	=	number of points for the dominant wavelength (wave packet test case)
n_b	=	number of points in the Gaussian half-width (wave packet test case)
p'	=	acoustic pressure
p_∞	=	ambient pressure
Re	=	Reynolds number
r_c	=	vortex radius
(r, θ)	=	polar coordinates (corotating-vortex test case)
St	=	Strouhal number
T_∞	=	ambient temperature
t	=	time
U_∞	=	freestream velocity
u	=	unknown function (scalar case)
u^n_j	=	numerical solution at $j\Delta x$ and $n\Delta t$
v_θ	=	tangential velocity (corotating-vortex test case)
(x_0, y_0)	=	coordinates of the center of the pulse or vortex
Y_m	=	Bessel function of the second kind and order m
α	=	Gaussian parameter (acoustic-pulse test case)
α_l, γ_l	=	coefficients of the Runge–Kutta scheme
Γ	=	circulation (corotating-vortex test case)
Δt	=	time step
Δx	=	spatial discretization step
δ	=	boundary-layer thickness
ε	=	amplitude (acoustic-pulse test case)
ζ	=	space integration variable (acoustic-pulse test case)
η	=	boundary-layer coordinate, $y\sqrt{Re_x}/x$
η_l	=	recurrence coefficients of OSp schemes
ν	=	kinematic viscosity
ξ	=	reduced wave number
$\xi^\star$	=	effective reduced wave number
ρ_∞	=	ambient density
σ	=	Courant–Friedrichs–Lewy number
$\phi^{p,\mathrm{TVD}}_j$	=	correcting term for total variation diminishing and monotonicity preserving
χ	=	filtering amplitude of dispersion-relation-preserving filter
Ω	=	angular velocity (corotating-vortex test case)
$\hat{\cdot}$	=	variable in Fourier space
$\lfloor\,\rfloor$	=	integer division symbol

Superscript

p	=	order of the scheme

Presented as Paper 2414 at the 12th AIAA/CEAS Aeroacoustics Conference, Cambridge MA, 8–10 May 2006; received 24 October 2006; revision received 12 June 2007; accepted for publication 18 June 2007.

*Assistant Professor, Laboratoire de Simulation Numérique en Mécaniques des Fluides; virginie.daru@paris.ensam.fr.

†Assistant Professor; Laboratoire de Simulation Numérique en Mécaniques des Fluides; xavier.gloerfelt@paris.ensam.fr. Member AIAA.

I. Introduction

THIS work is motivated by the desire to design numerical methods that combine a high accuracy on a large range of wave numbers and the ability to capture shock waves. These properties are needed to describe supersonic turbulent flows with large eddy simulation or aeroacoustic phenomena that occur in shocked flow, such as the screech tone in underexpanded jets, the shock/boundary-layer interactions on transonic airfoils, or the supersonic cavity flows for military aircraft. The centered finite difference schemes associated with a selective filtering technique, classically used in computational aeroacoustics (CAA) [1–5], fail to describe

discontinuities. The spurious oscillations generated may deteriorate the acoustic solution, for which the amplitude is very low. On the other hand, classical second-order shock-capturing schemes are far too dissipative and will alter the propagation features of the acoustic waves. It is desirable to use a scheme that can both represent short-wavelength perturbations with a minimum of numerical dispersion and dissipation and capture discontinuities with robustness.

To this aim, essentially nonoscillatory (ENO) and weighted ENO (WENO) schemes have encountered some success since their introduction in 1987 [6]. They are based on the use of adaptive stenciling. Several attempts have been made to extend this family of schemes to CAA. Casper and Meadows [7] proposed a modification of the stencil-biasing procedure to improve the accuracy, with illustration of a shock–vortex interaction. Adams and Shariff [8] developed compact ENO schemes to allow a spectral-like resolution while dissipating nonresolved wave numbers. Ekaterinaris [9] compared WENO schemes and compact finite difference schemes combined with characteristic-based filters applied to aeroacoustic test cases on curvilinear meshes. Deng and Zhang [10] discussed weighted compact nonlinear schemes that combine high order in smooth regions and can capture discontinuities robustly. Optimized ENO/WENO schemes were derived by Wang and Chen [11] with a dispersion-relation-preserving (DRP)-type optimization to minimize dispersion and dissipation errors. Another possibility to combine high-order and shock-capturing properties consists of optimizing finite volume schemes [12–14]. Popescu et al. [15] proposed to directly extend DRP or compact finite difference schemes to a finite volume context. The class of arbitrary high-order schemes using derivatives (ADER) finite volume or ADER discontinuous Galerkin methods has also been tested in CAA [16,17].

In the present study, we propose to test the ability of a recently introduced family of upwind-limited schemes [18] in the developing area of CAA. The schemes presented in the first section offer a compromise between high accuracy in smooth regions and an efficient shock-capturing technique. A Fourier analysis is conducted for the scalar case of the advection equation in the second section and is compared with the 11-point-stencil DRP scheme of Bogey and Bailly [5]. The high accuracy is then tested in two dimensions for several test problems: a subsonic acoustic problem, the viscous interaction of two corotating vortices, the growth of a supersonic boundary layer, and an inviscid shock–vortex interaction. The final illustration concerns a supersonic flow over a rectangular cavity, which involves moving discontinuities.

II. Description of the Schemes

A. One-Step Monotonicity-Preserving Schemes

These schemes were developed in [18]. We recall the principle of their construction and give a general recurrence formula for a pth-order accurate scheme. We also describe the procedure of limitation they can be equipped with to obtain a nonoscillating total-variation-diminishing (TVD) or monotonicity-preserving (MP) scheme.

In the linear scalar case of a transport equation,

$$u_t + a u_x = 0 \quad \text{with } a > 0 \tag{1}$$

where u is the unknown function of (x, t) and a is the convection speed. Let us consider the explicit scheme of order p:

$$u_j^{n+1} = u_j^n - \frac{\Delta t}{\Delta x}\left(F_{j+1/2}^p - F_{j-1/2}^p\right) \tag{2}$$

where u_j^n is the numerical solution at point $(j\Delta x, n\Delta t)$ and $F_{j+1/2}^p$ is the numerical flux. A general scheme of the required order of accuracy is constructed by following the modified equation approach: given a scheme of order p, the modified equation of this scheme can be established, and a scheme of order $p+1$ is obtained by correcting the leading error term in this equation.

To give an example, let us write the numerical flux of the second-order Lax–Wendroff scheme as

$$F_{j+1/2}^2 = a u_j^n + \frac{1-\sigma}{2} a\left(u_{j+1}^n - u_j^n\right)$$

where σ is the Courant–Friedrichs–Lewy (CFL) number $\sigma = a\Delta t/\Delta x$. The modified equation of this scheme is

$$u_t + a u_x = -a\frac{\Delta x^2}{6}(1-\sigma^2)u_{xxx} \tag{3}$$

where u_{xxx} denotes the third-order derivative of u. The numerical flux of a third-order upwind scheme can be obtained by subtracting from the Lax–Wendroff flux a term discretizing the right-hand side of Eq. (3). The third-order flux reads

$$F_{j+1/2}^3 = F_{j+1/2}^2 - \frac{(1-\sigma)}{2}\frac{(1+\sigma)}{3} a\left(u_{j+1}^n - 2u_j^n + u_{j-1}^n\right)$$

By recursively pursuing this procedure, a general recurrence relation for the derivation of a $(p+1)$th-order numerical flux from a pth-order flux can be written. A minimum stencil is obtained by following a general rule of discretizing odd derivatives using upwind formulas and even derivatives using centered formulas. In view of a spatial reconstruction approach, it can also be shown that this rule minimizes the error associated with the spatial reconstruction. The recurrence relation for $p \geq 1$ is

$$F_{j+1/2}^{p+1} = F_{j+1/2}^p + a\eta_{p+1}\sum_{l=0}^{p}(-1)^l \mathbf{C}_p^l u_{j+m-l} \tag{4}$$

where $m = \lfloor (p+1)/2 \rfloor$ ($\lfloor\ \rfloor$ is the integer division symbol), $\mathbf{C}_p^l = p!(p-l)!/l!$, and

$$\eta_l = \prod_{q=2}^{l}(-1)^q \frac{\lfloor q/2 \rfloor - (-1)^q\sigma}{q} \tag{5}$$

Notice that this family of schemes is coupled in time and space and have the same order of accuracy in time and space. All of these schemes are stable under the usual CFL condition $\sigma \leq 1$. Moreover, they give the exact solution for $\sigma = 1$.

These schemes should be corrected to get good shock-capturing properties. To this end, the numerical flux can be modified to satisfy the TVD conditions derived by Harten [19], in the form

$$F_{j+1/2}^{p,\mathrm{TVD}} = f_j^n + \phi_j^{p,\mathrm{TVD}} \cdot \frac{1-\sigma}{2}\left(f_{j+1}^n - f_j^n\right)$$

with

$$\phi_j^{p,\mathrm{TVD}} = \max\left\{0, \min\left(\frac{2}{1-\sigma}, \frac{2}{1-\sigma}\frac{F_{j+1/2}^p - f_j^n}{f_{j+1}^n - f_j^n}, \frac{2r_j}{\sigma}\right)\right\}$$

where $f_j^n = a u_j^n$ and $r_j = (u_j^n - u_{j-1}^n)/(u_{j+1}^n - u_j^n)$. The TVD scheme obtained in this way will, however, exhibit the deficiency inherent to the TVD concept, which is the clipping of local extrema induced by the local degeneracy to first order of the scheme in these areas. By relaxing the TVD conditions into MP conditions in the vicinity of local extrema, one can obtain a nonoscillatory scheme while preserving the high order of accuracy in smooth parts of the solution. The MP conditions were first introduced in [20] in a geometrical framework and reformulated in [18] as extended TVD conditions. In brief, let us say that these conditions enlarge the TVD bounds constraining the numerical solution in regular zones. The TVD conditions constrain the numerical flux of the high-order scheme to stay inside the intersection of the intervals $[f_j^n, f_{j+1}^n]$ and $[f_j^n, f_j^{\mathrm{ul}}]$, where $f_j^{\mathrm{ul}} = f_j^n + [(1-\sigma)/\sigma](f_j^n - f_{j-1}^n)$. The MP conditions provide an enlargement of these intervals by introducing the values f_j^{md} and f_j^{lc}, given by

$$f_j^{\mathrm{md}} = f_j^n + \tfrac{1}{2}\left(f_{j+1}^n - f_j^n\right) - \tfrac{1}{2}d_{j+1/2} \tag{6}$$

$$f_j^{\mathrm{lc}} = f_j^n + \frac{1}{2}\left(f_{j+1}^{ul} - f_j^n\right) + \frac{1}{2}\frac{(1-\sigma)}{\sigma} d_{j-1/2} \tag{7}$$

where $d_{j+1/2}$ is a curvature term given by

$$d_{j+1/2} = \min \mathrm{mod}(f_{j+1} - 2f_j + f_{j-1}, f_{j+2} - 2f_{j+1} + f_j)$$

It can be shown that these conditions preserve the original high-order scheme (4) everywhere except in the vicinity of discontinuities, in which they are equivalent to the TVD conditions. More details can be found in [18]. Convergence results for the linear scalar case and smooth initial data were reported in [18], demonstrating that the MP scheme gives the same results as the unlimited scheme, contrary to the TVD scheme, which severely degrades the initial order of accuracy (scheme (4) is named OSp for one-step pth-order accurate, with OSTVDp and OSMPp for the TVD or MP versions).

For the aeroacoustic applications treated here, we have introduced a small modification of the MP conditions, which allows numerical oscillations at the order of Δx for CFL values lower than 0.5. The modified values f_j^{md} and f_j^{lc} are obtained by multiplying the curvature terms in Eqs. (6) and (7) by a factor $1 + \tau(u_{j+1}^n - u_j^n)$, where $\tau = \max[25 \cdot (0.5 - \sigma), 0]$. This modification allows accurate results for the whole range of the CFL numbers in all of the difficult cases we have treated. At the same time, the good nonoscillatory behavior of the scheme is not altered.

In the nonlinear system case, a local linearization of the Roe type is applied to obtain a practicable scheme. Moreover, in the multidimensional case, the scheme is implemented using Strang splitting. This reduces the formal accuracy of the schemes to second order. However, numerical experiments show that a very low level of error is still achieved, as will be illustrated in the following.

B. Dispersion-Relation-Preserving Schemes

The standard CAA algorithm used for the comparison is based on a finite difference scheme for spatial discretization and a Runge–Kutta algorithm for time advancement, both optimized in the wave-number space by following the DRP procedure of Tam and Webb [2].

The explicit finite difference scheme with an 11-point stencil, optimized by Bogey and Bailly [5], is used. A spatial derivative is approximated as

$$\left.\frac{\partial u}{\partial x}\right|_j = \frac{1}{\Delta x}\sum_{l=-5}^{5} a_l u[(j+l)\Delta x]$$

For a centered stencil, the scheme is nondissipative and is formally fourth-order accurate. By applying a spatial Fourier transform, the effective wave number is

$$k^\star \Delta x = 2\sum_{l=1}^{5} a_l \sin(lk\Delta x) \tag{8}$$

The governing equations are integrated in time using an explicit low-storage six-step Runge–Kutta scheme, for which the dispersion and dissipation errors were minimized in the frequency space [5]:

$$u_j^0 = u_j^n \qquad u_j^l = u_j^n + \alpha_l \Delta t f_j^{l-1} \quad (l = 1, \ldots, 6), \qquad u_j^{n+1} = u_j^6$$

where the superscript n denotes the iteration number. To avoid spurious grid-to-grid oscillations, a selective filtering is applied after each complete time step. These numerical oscillations originate from unresolved perturbations and any discontinuity, such as the boundary conditions, very stiff gradients, or shock waves. They must be eliminated to prevent the divergence of the numerical procedure. A filtered quantity u_j^f is computed by using a centered filter built on an 11-point stencil [5]:

$$u_j^f = u_j - \chi D_j^f \tag{9}$$

where

$$D_j^f = \sum_{l=-5}^{5} d_l u[(j+l)\Delta x]$$

and the coefficient χ is between zero and one (it is fixed at 0.2 throughout the study). The filter has symmetric coefficients d_l so that it is nondispersive, and the dissipation error is minimized in the wave-number space.

III. Analysis for the Scalar Case

The linear scalar case of transport (1) is considered to evaluate the dispersion and dissipation errors of the unlimited OSp family of schemes and to quantify their limit of accuracy and resolvability in comparison with the DRP scheme.

A. Fourier Analysis

1. *One-Step Monotonicity-Preserving Schemes*

Considering a single harmonic $\hat{u}^n \mathrm{e}^{ij\xi}$, the amplification factor $G = \hat{u}^{n+1}/\hat{u}^n$ of scheme (2) is

$$G_{\mathrm{OS}p} = 1 - \sigma(1 - e^{-i\xi})\left[1 + \sum_{q=1}^{p-1}\eta_{q+1}\sum_{l=0}^{q}(-1)^l \mathbf{C}_q^l e^{i(m-l)\xi}\right] \tag{10}$$

where η_q is given by Eq. (5), $m = \lfloor p/2 \rfloor$, and $\xi = k\Delta x$ is the reduced wave number. For comparison with the exact amplification factor, $G_{\mathrm{OS}p}$ is written as $|G_{\mathrm{OS}p}(\xi)|e^{-i\sigma\xi^\star}$, where $|G|$ represents the amplification rate and $\xi^\star$ is the effective reduced wave number. The dissipation error is then defined as $1 - |G|$ and the dispersion (or phase) error is $\xi - \xi^\star$.

2. *Dispersion-Relation-Preserving Schemes*

In the linear case of Eq. (1), the Runge–Kutta algorithm is developed as

$$u_j^{n+1} = u_j^n + \sum_{l=1}^{6}\gamma_l \Delta t^l \frac{\partial^l u_j^n}{\partial t^l} + \mathcal{O}(\Delta t^6) \tag{11}$$

where

$$\gamma_l = \prod_{q=6-l+1}^{6} \alpha_q$$

By applying a Fourier transform to Eq. (11) and taking Eq. (8) into account, we write the amplification factor for Eq. (1) as

$$g_{\mathrm{DRP}}(\xi) = \frac{\hat{u}_j^{n+1}}{\hat{u}_j^n} = 1 + \sum_{l=1}^{6}\gamma_l \sigma^l \left(-2i\sum_{q=1}^{5} a_q \sin(q\xi)\right)^l$$

The filter transfer function is obtained by applying a Fourier transform to Eq. (9):

$$\hat{D}^f(\xi) = d_0 + \sum_{l=1}^{5} 2d_l \cos(l\xi)$$

The filtering operation (9) corresponds to a convolution operation in physical space, so that the amplification factor after filtering is multiplied by $1 - \chi\hat{D}^f$:

$$G_{\mathrm{DRP}}(\xi) = \left(1 + \sum_{l=1}^{6}\gamma_l \sigma^l \left[-2i\sum_{q=1}^{5} a_q \sin(q\xi)\right]^l\right)[1 - \chi\hat{D}^f(\xi)] \tag{12}$$

3. *Errors of Dispersion and Dissipation*

The dispersion and dissipation errors deduced from their amplification factors are analyzed for the OS7, OS11, and DRP schemes. The effective wave number and the modulus of the amplification factor are represented in Fig. 1 as functions of the

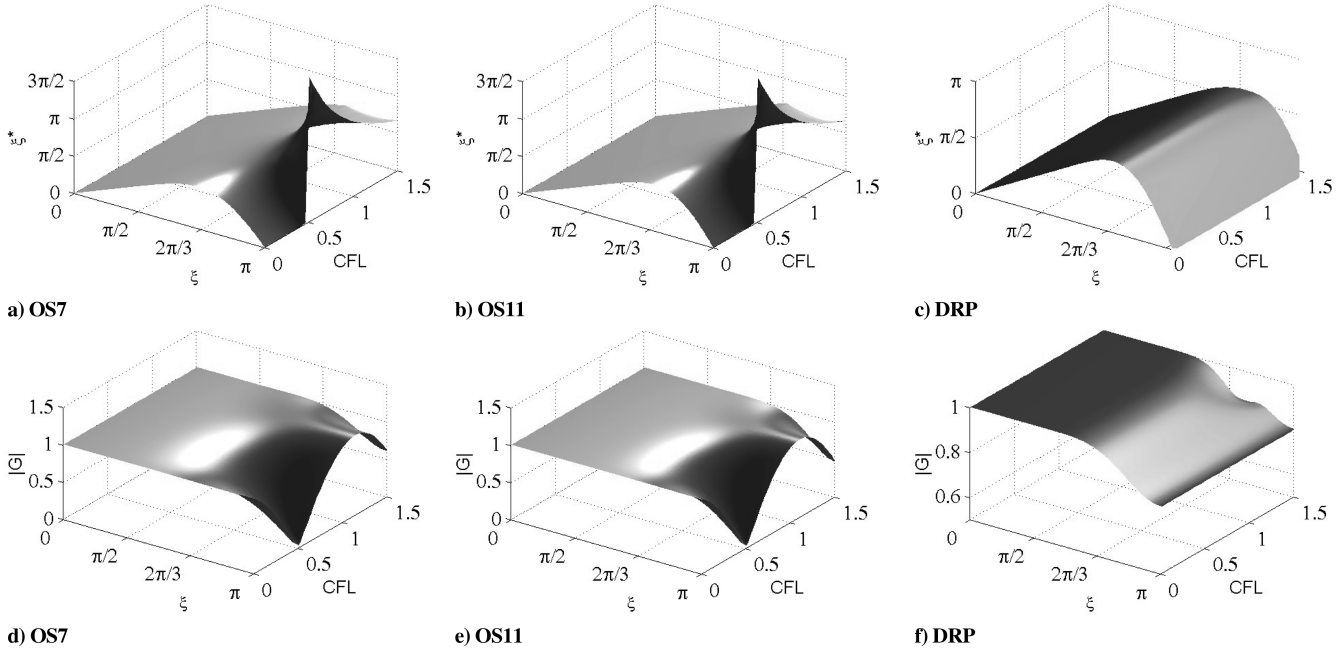

Fig. 1 Effective reduced wave number ξ^* (top) and amplification rate $|G|$ (bottom) for the OS7 (left), OS11 (middle), and DRP (right) schemes as functions of the reduced wave number ξ and CFL number σ.

reduced wave number ξ and the CFL number σ. All of the schemes have a comparable behavior in the low-frequency range, with a low level of error. The main differences are located in the high-wave-number zone $\pi/3 \leq \xi \leq \pi$, in which the OSp errors are much more dependent on the CFL number. These types of schemes are exact for $\sigma = 1$, have no dispersion, and have a maximum of dissipation for $\sigma = 0.5$.

Several slices of the surfaces are depicted in Fig. 2 for fixed values of the CFL number. The modified wave number and the modulus of the amplification factor of the different schemes, together with their dissipative and dispersive errors, are presented. The logarithmic scale used to represent the errors clearly shows that for all schemes, the dispersion is maintained at a very low level up to the limit of resolvability $\xi \simeq \pi/2$, corresponding to four points per wavelength. The OSp schemes for $\sigma < 0.5$ and the DRP schemes for all CFL are not able to treat grid-to-grid oscillations $\xi = \pi$ (i.e., two points per wavelength, or the Nyquist limit). These spurious oscillations are eliminated in the DRP schemes by introducing artificial dissipation to prevent the divergence of the numerical procedure. This dissipation must act only on the waves that are not accurately resolved by the scheme $\xi > \pi/2$. Both OS7 and OS11 compare well with DRP, considering the dissipative and dispersive errors. OS11 has the best properties, giving almost spectral accuracy for ξ slightly lower than $\pi/2$ (i.e., four points per wavelength). The DRP scheme is slightly better near $\xi = \pi/2$, but has a nonnegligible residual level of errors for low frequencies, due to the DRP optimization. The dissipation is essentially induced by the filter. Note that for $\sigma = 1.1$, the dissipation error of OSp is not represented, because $|G_{\mathrm{OS}p}| > 1$ and the scheme is unstable. The upper limit for OSp schemes is thus $\sigma = 1$.

B. Advection of a Wave Packet

An initial wave packet is defined by

$$u(x) = \sin\left(\frac{2\pi x}{n_a \Delta x}\right) \exp\left[-\ell_n 2\left(\frac{x}{n_b \Delta x}\right)^2\right]$$

where $n_a \Delta x$ is the dominant wavelength and $n_b \Delta x$ is the Gaussian half-width, propagated over a distance of $200\Delta x$. This test case is a typical problem to study long-range propagation of disturbances discretized by few points [5]. The wavelength of the initial perturbation is discretized by six points ($n_a = 6$ and $n_b = 9$). The results are presented in Fig. 3 for three values of the CFL number: $\sigma = 0.3$, $\sigma = 0.5$, and $\sigma = 0.7$. Both the OS11 and DRP schemes give a nearly perfect solution, whatever the CFL number. The OS7 scheme is slightly more dissipative, but the solution is still acceptable. Figure 4 shows the effect of the MP limiter on the OS7 and OS11 schemes. The conclusion is that the MP limiter leaves the numerical solution (given by the unlimited scheme for the tested CFL numbers) nearly unchanged.

This scalar test case shows that the OS7 and OS11 schemes are good candidates for the advection of high-frequency perturbations and that the MP procedure of limitation does not add unwanted dissipative effects when the solution is smooth. However, as mentioned earlier, in the nonlinear case, the order of accuracy of the OSp schemes is not preserved. In the following, their ability to accurately solve the Euler and Navier–Stokes equations is analyzed.

IV. Test Cases

A. Gaussian Acoustic Pulse

The first test case is the propagation in ambient air at rest of an acoustic pulse generated by an initial pressure disturbance with a Gaussian spatial distribution:

$$p'(x, y, t = 0) = \varepsilon \times \exp\{-\alpha[(x - x_0)^2 + (y - y_0)^2]\}$$

where $\alpha = \ell_n 2/b^2$. The variables are nondimensionalized by a length scale Δ, a velocity scale c_∞, a time scale Δ/c_∞, a density scale ρ_∞, and a pressure scale $\rho_\infty c_\infty^2$, where c_∞ and ρ_∞ denote, respectively, the ambient sound speed and density. The pulse is centered at $x_0 = 0$ and $y_0 = 0$ in a square domain defined by $-50 \leq x, y \leq 50$. The 2-D Euler equations are solved on a uniform $N \times N$ Cartesian mesh grid. The Gaussian half-width is taken at $b = 3$ and the amplitude is $\varepsilon = 10^{-5}$. The analytical solution of this initial value problem is given in [21]

$$p'_{\mathrm{exact}}(x, y, t) = \frac{\varepsilon}{2\alpha} \int_0^\infty \exp\left(-\frac{\zeta^2}{4\alpha}\right) \cos(t\zeta) J_0(\zeta r) \zeta \, \mathrm{d}\zeta$$

where J_0 is the Bessel function of the first kind and order zero, and $r = \sqrt{(x - x_0)^2 + (y - y_0)^2}$.

Nonreflecting conditions are required to avoid spurious reflections that can superpose onto the physical waves. To this end, the radiation boundary conditions of Tam and Dong [22], using a polar asymptotic solution of the linearized Euler equations in the acoustic far field, are

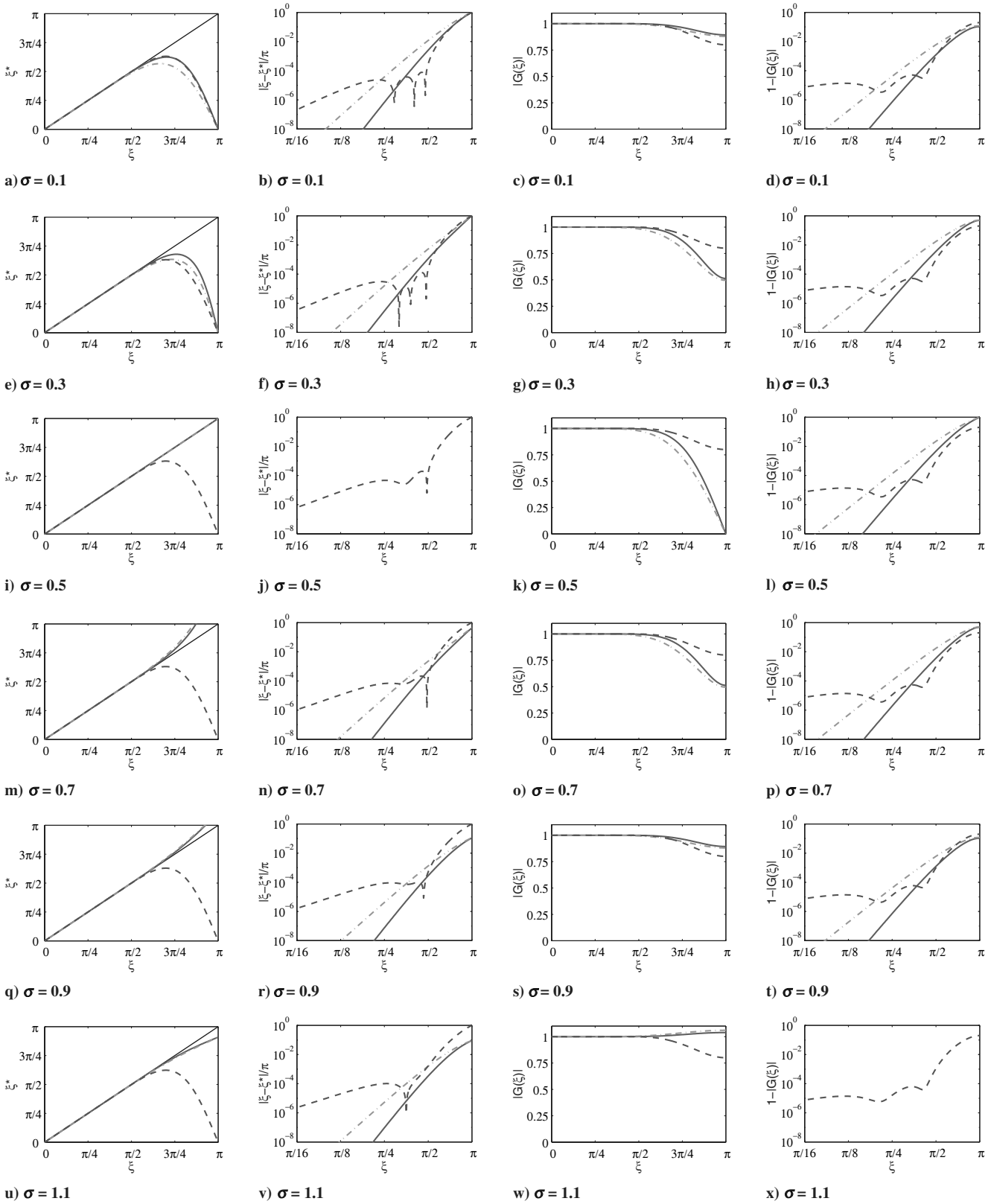

Fig. 2 Effective wave number, dispersive error, modulus of the amplification factor, amplitude error (from left to right); OS11 (solid), OS7 (dashed-dotted), and DRP (dashed) schemes.

applied at the boundaries of the computational domain. The results are presented for $N = 101$, 51, and 25 at two nondimensionalized times $t = 24$ and 48, before and after the pulse has reached the boundaries. The CFL number is equal to 0.5, corresponding to $\Delta t = 0.5$, 2 and 1, respectively.

Two very-low-level isocontours of the fluctuating pressure are plotted in Fig. 5 at $t = 24$ and in Fig. 6 at $t = 48$. These instantaneous views show the spatial distribution of the error for the intermediate mesh $N = 51$. The phase shift is weak for both schemes, even for the lowest level $p' = 10^{-9}$. At $t = 48$, the pulse has reached the boundaries and no reflected wave is visible. The comparison between the different meshes is done in Fig. 7. The 25×25 grid is a very difficult case and the solutions are badly discretized, with bigger errors noticed for the DRP scheme, notably at $t = 48$. On the

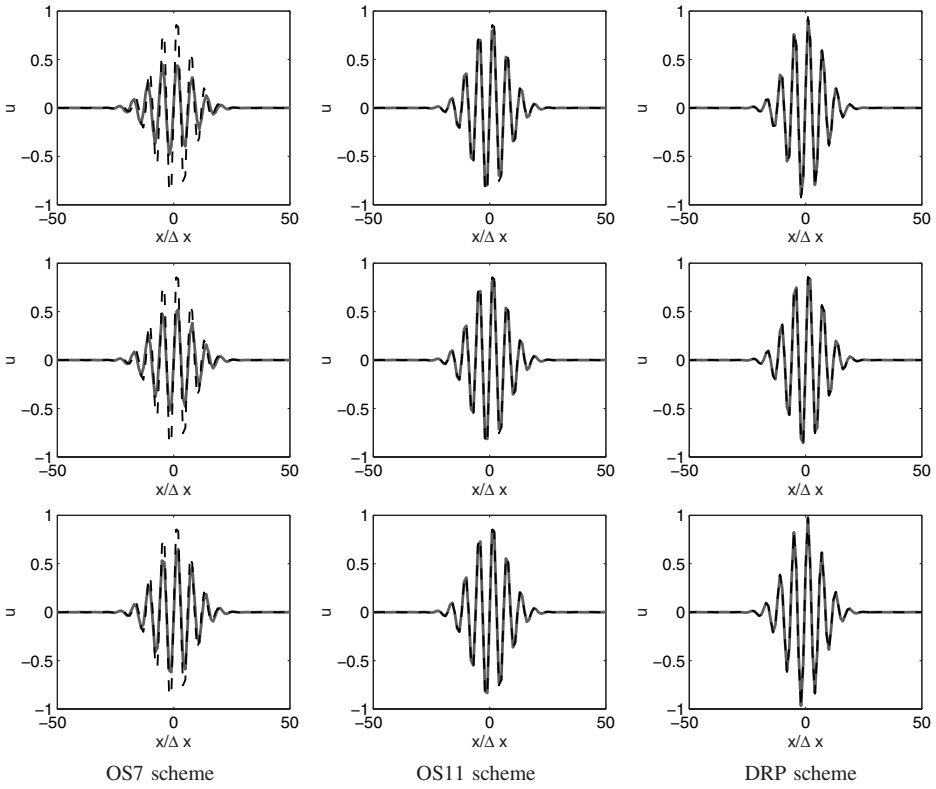

Fig. 3 Advection of a wave packet; solution propagated over a distance of $200\Delta x$ (solid) compared with the analytical solution (dashed); results with $\sigma = 0.3$ (first row), $\sigma = 0.5$ (second row), and $\sigma = 0.7$ (third row); initial wave packet wavelength discretized by six points.

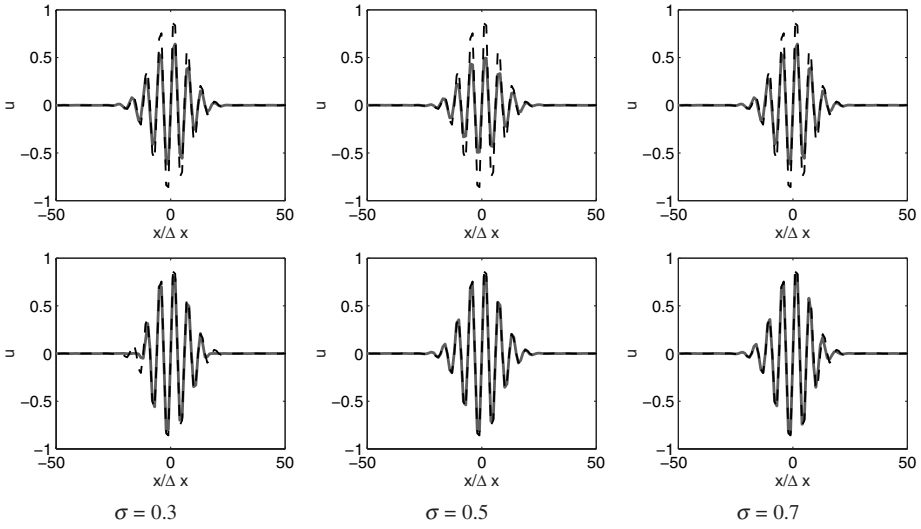

Fig. 4 Advection of a wave packet; influence of the MP condition on the numerical solution (solid) compared with the analytical solution (dashed); six points per wavelength with OSMP7 scheme (top) and OSMP11 scheme (bottom).

contrary, for the finer grid of 101×101 points, OSMP11 results are less accurate. All of these visual conclusions are confirmed by the errors calculated with the L2-norm and reported in Table 1, showing second-order convergence for OSMP11 and fourth-order convergence for DRP, as mentioned earlier.

Concerning the CPU times needed by the two methods, one finds 1.687 s for the DRP scheme and 2.531 s for the OSMP11 scheme to reach $t = 48$ on the 101×101 grid. OSMP11 is therefore 50% more expensive than DRP. The supplementary cost is essentially associated with the multiple tests needed by the MP procedure. For comparison, it has been shown in [18] that the OSMP7 scheme is roughly five times less expensive than a WENO5 scheme associated with a third-order TVD Runge–Kutta scheme.

B. Sound Emission by a Corotating Vortex Pair

The second test case concerns the acoustic field induced by the viscous interaction of two corotating vortices in air at rest, which has previously been studied theoretically [23–25] and numerically [26–29].

Two vortices each of circulation Γ separated by a distance $2l$ rotate about the x_3 axis midway between them at angular velocity $\Omega = \Gamma/4\pi l^2$, as seen in Fig. 8. The rotation Mach number is $M_r = \Gamma/(4\pi l c_\infty)$. The vortex-core is described by the Scully [30] model:

$$v_\theta(r) = -\frac{\Gamma r}{2\pi\left(r_c^2 + r^2\right)}$$

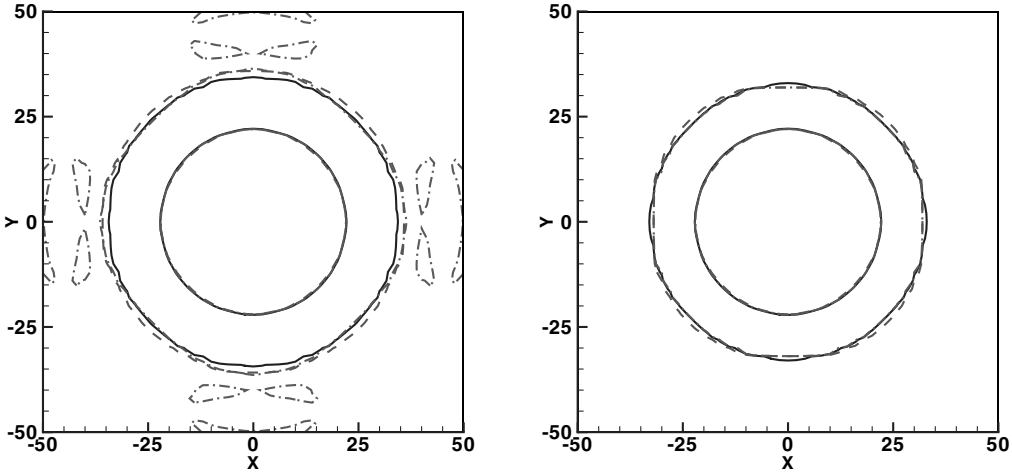

Fig. 5 Acoustic-pulse test case at $t = 24$ ($N = 51$); pressure isocontours $p' = 10^{-9}$ (left) and $p' = 10^{-8}$ (right); OS11 scheme (dashed), DRP scheme (dashed-dotted), and analytical solution (solid).

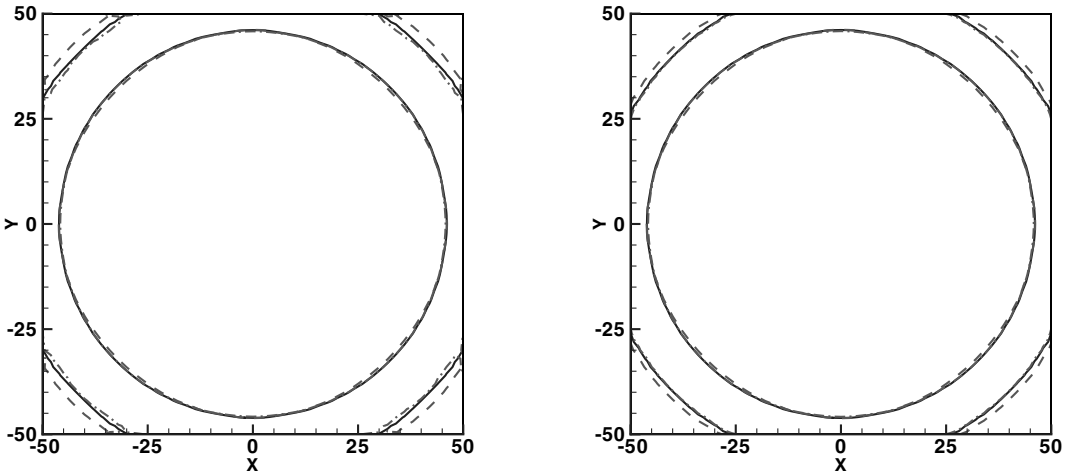

Fig. 6 Acoustic-pulse test case at $t = 48$ ($N = 51$); pressure isocontours $p' = 10^{-9}$ (left) and $p' = 10^{-8}$ (right); OS11 scheme (dashed), DRP scheme (dashed-dotted), and analytical solution (solid).

where v_θ is the initial tangential velocity distribution of each vortex, r is the radial distance from the vortex center, and a is the vortex radius. The Mach number based on the maximum tangential velocity $M = \Gamma/(4\pi r_c c_\infty)$ is 0.5, where $r_c/l = 2/9$ and $M_r = 1/9$. The Reynolds number $Re = \Gamma/\nu$ is equal to 114,000, where $\nu = 1.5 \times 10^{-5}$ kg/m^2 is the kinematic viscosity. The ambient air conditions are $p_\infty = 1$ atm and $T_\infty = 298.15$ K.

The Navier–Stokes equations are discretized on a 341×341 nonuniform Cartesian mesh grid. From the origin at the center of the domain and in each direction, the grid size is regular over 60 points with $\Delta x = 2 \times 10^{-4}$ m and is then stretched with a rate of 4% until the boundaries located at $\pm 110l$ are reached. This kind of grid is typical of aeroacoustic problems, with a disparity of scales between the vortices and the corresponding sound field. The time steps are 2.02×10^{-7} s for the OSMP11 scheme and 4.54×10^{-7} s for the DRP scheme. The flow is initially specified as solenoidal to reduce the magnitude of the initial acoustic transient. This is done by first solving an incompressible Poisson equation for the pressure:

$$p_{,ii} = -\rho_\infty u_{i,j} u_{j,i}$$

The temporal evolution of the pressure is presented in Fig. 9a. Several regular rotation cycles are observable, and the vortices are not yet in the merging phase. The typical double spiral pattern of a rotating quadrupolar source is observed with both schemes, as seen in Fig. 10 at $t = 5 \times 10^{-3}$ s. A quantitative comparison between the results obtained with the two schemes is proposed in Fig. 9b. The pressure profiles along $y = 0$ are superimposed with the following analytical solution [26]:

$$p'(r, \theta, t) = \frac{-\rho_\infty \Gamma^4}{64\pi^3 l^4 c_\infty^2} \left[J_2\left(\frac{2\Omega r}{c_\infty}\right) \sin(2\theta + 2\Omega t) + Y_2\left(\frac{2\Omega r}{c_\infty}\right) \cos(2\theta + 2\Omega t) \right] \tag{13}$$

where J_2 and Y_2 are the Bessel function of order two, respectively, of the first and second kind. This solution is obtained using vortex sound theory for inviscid point vortices. The wavelength is comparable with that from the simulations. The amplitudes of the acoustic waves are close for the two schemes, but are slightly lower than the theoretical value. This discrepancy is certainly related to the spread distribution of the vortices in the simulations. Once again, it can be seen that the comparison between the results obtained using OSMP11 and DRP schemes is satisfactory.

C. Growth of a Supersonic Laminar Boundary Layer

The schemes OSMP7 and DRP are now applied to the computation of the laminar flow over a flat plate at $M = 2$ and $Re = 10^5$ per unit length. The supersonic regime is considered because the solution is less dependent on the choice of the inlet and outlet boundary conditions than in the subsonic case, which allows focus on the comparison of the two numerical methods. The computational domain defined by $0 \le x \le 4$, $0 \le y \le 0.16$ is discretized by a uniform Cartesian grid with 120 points along the x

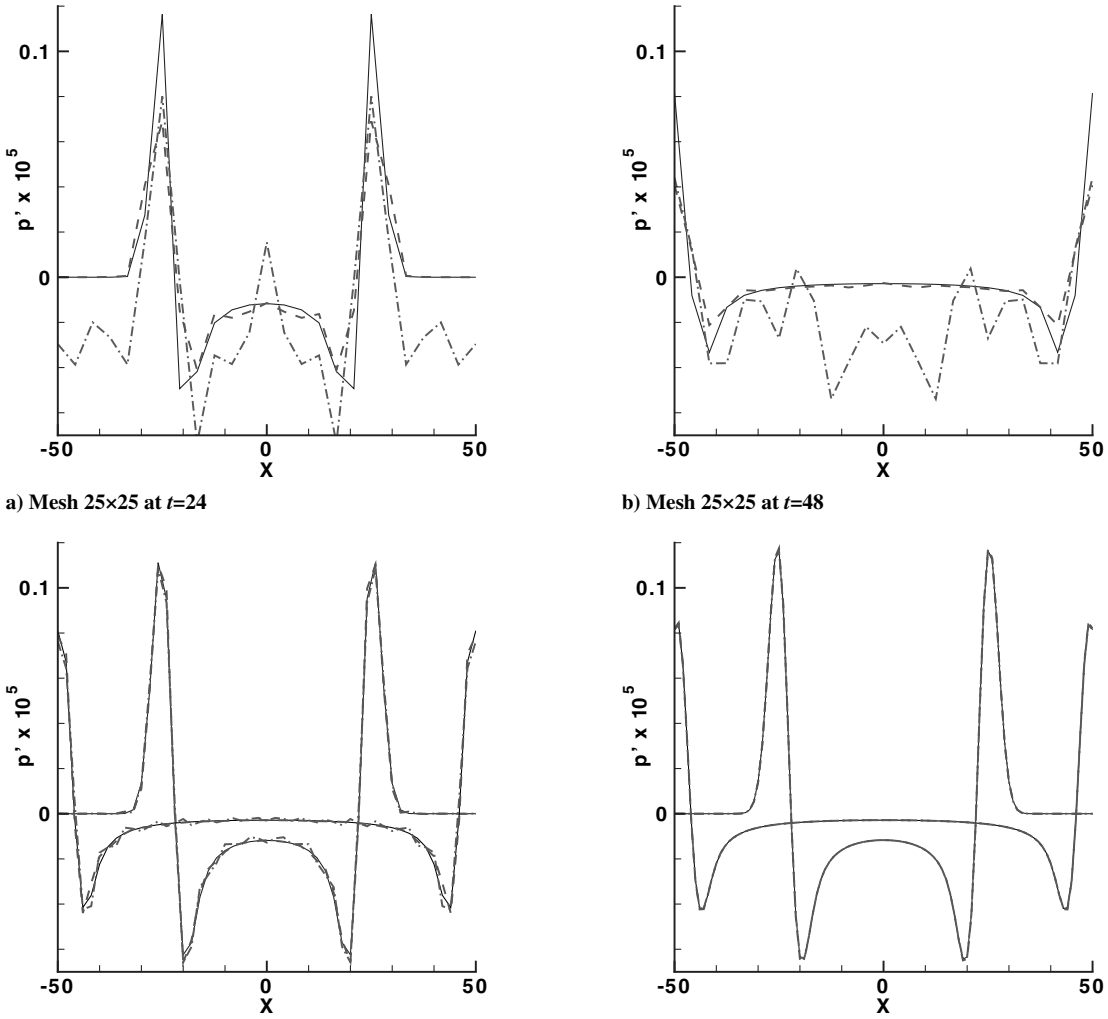

a) Mesh 25×25 at t=24

b) Mesh 25×25 at t=48

c) Mesh 51×51 at t=24 and 28

d) Mesh 101×1011 at t=24 and 48

Fig. 7 Pressure profiles for the acoustic-pulse test case; OS11 scheme (dashed), DRP scheme (dashed-dotted), and analytical solution (solid).

axis. The direction normal to the plate is discretized by 20, 40, or 80 points, yielding, respectively, about 42, 16, or 5 points in the boundary layer at the exit station. The three meshes are referred to as the fine, medium, and coarse grids.

All of the freestream values are imposed at $x = 0$ (supersonic inlet). A first-order extrapolation of the conservative variables (supersonic outlet) is used at the exit plane and at the upper boundary. An adiabatic condition is prescribed at the wall by using ghost points for the variables. These ghost points use the values of the variables at the first grid point, and their number allows the application of the same scheme as for the interior points. To assess the accuracy properties of the OSMP7 and DRP for this viscous test case, the streamwise velocity and temperature profiles computed at station $x = 3$ are plotted in Figs. 11 and 12 versus the boundary-layer coordinate $\eta = y\sqrt{Re_x}/x$ and compared with a reference solution obtained from a boundary-layer code that solves the boundary-layer equations using a space-marching technique. On the fine and medium grids, the two schemes yield profiles in very good agreement with the reference solution. On the coarse grid, they are still able to provide an acceptable solution, with no more than five points in the boundary layer. The velocity profile is better captured by the DRP scheme, but both schemes show little errors for the prediction of the recovery temperature. These errors are related to the presence of shock waves emanating from the stepwise growth of the boundary layer from one to two points or from two to three points, which can perturb the downstream profiles.

D. Two-Dimensional Shock–Vortex Interaction

This test case considers the inviscid interaction of a plane weak shock with a single isentropic vortex (it was treated in [18] in the viscous case).

The domain has a dimension of $[0, 2] \times [0, 2]$. A stationary plane shock is located at $x = 1$. The prescribed pressure jump through the

Table 1 Acoustic-pulse test case. L_2 error over the whole computational domain at $t = 24$ and $t = 48$

Scheme	Number of grid points	L_2 error $t = 24$	L_2 error $t = 48$
OSMP11	25×25	1.296%	1.499%
	51×51	0.292%	0.521%
	101×101	0.074%	0.146%
DRP	25×25	2.1486%	2.817%
	51×51	0.1252%	0.2227%
	101×101	0.0074%	0.0141%

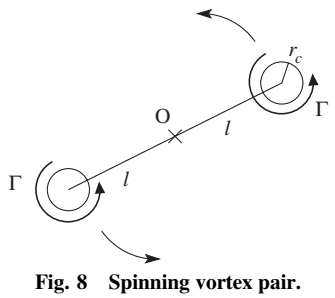

Fig. 8 Spinning vortex pair.

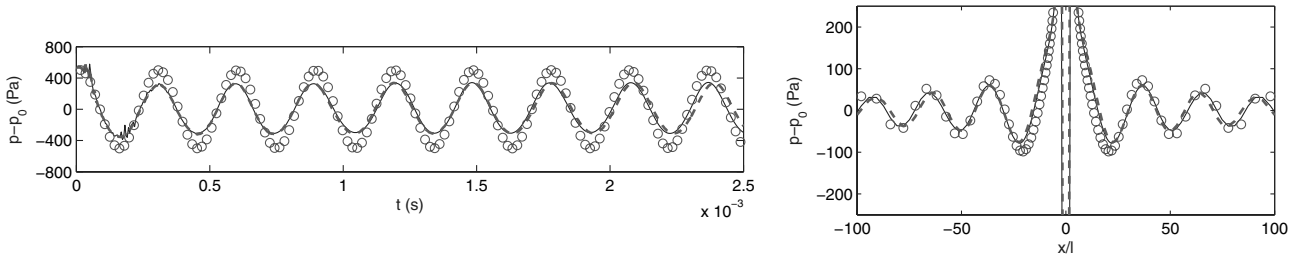

a) b)

Fig. 9 Corotating-vortex-pair test case: a) time trace of the pressure at ($x/l = -4.1$, $y = 0$) with temporal mean removed for the OSMP11 scheme (dashed) and DRP scheme (solid) and b) pressure profiles at $t = 5 \times 10^{-3}$ s along $y = 0$ for the OSMP11 scheme (dashed), DRP scheme (solid), and analytical solution (13) (o).

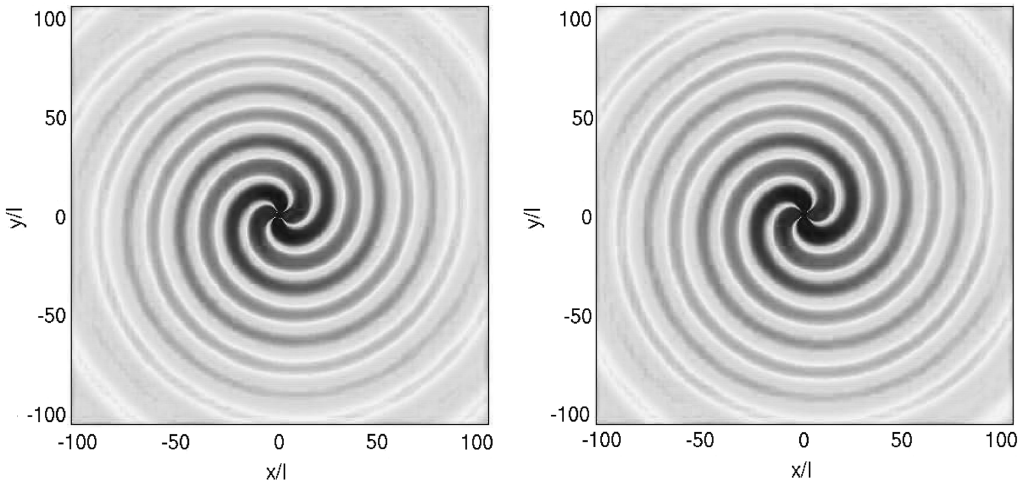

Fig. 10 Corotating-vortex-pair test case; contour plot of the fluctuating pressure field (temporal mean p_0 removed) at $t = 5 \times 10^{-3}$ s; OSMP11 scheme (left) and DRP scheme (right).

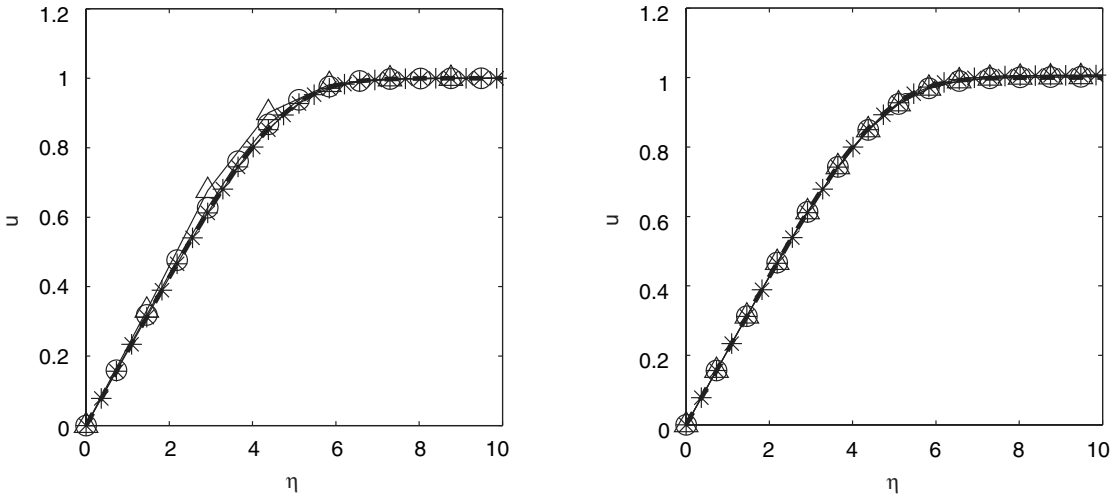

Fig. 11 Supersonic laminar boundary layer; effect of grid coarsening on the streamwise velocity profile at station $x = 3$ for the OSMP7 (left) and DRP (right) schemes; fine grid (-*-), medium grid (-○-), coarse grid (-△-), and reference solution (dashed).

shock is $\Delta p/p_\infty = 0.4$, where p_∞ is the static pressure at infinity, corresponding to a reference Mach number $M_0 = 1.1588$. An isolated Taylor vortex centered at $(x_0, y_0) = (\frac{1}{2}, 1)$ is initially superimposed on the base flow. The tangential velocity in the vortex is given by

$$v_\theta(r) = C_1 r \cdot e^{-C_2 r^2} \tag{14}$$

with

$$C_1 = \frac{U_c}{r_c}, \qquad C_2 = \frac{1}{2r_c^2}, \qquad r = \sqrt{(x - x_0)^2 + (y - y_0)^2}$$

The calculations were performed for $r_c = 0.075$ and $U_c = 0.25$. Periodic boundary conditions are applied in the y direction. The computations stopped at a dimensionless time $t = 0.72$.

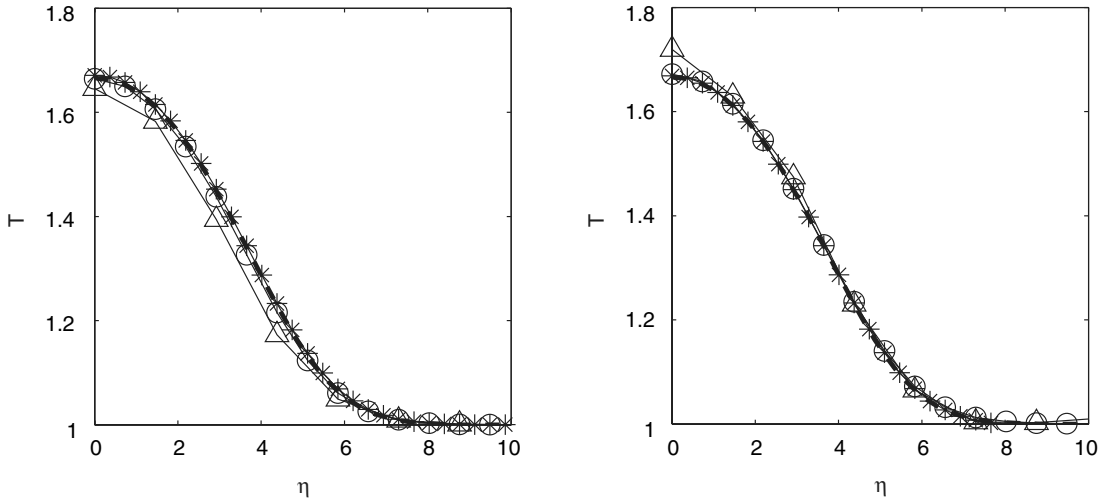

Fig. 12 Supersonic laminar boundary layer; effect of grid coarsening on the temperature profile at station $x = 3$ for the OSMP7 (left) and DRP (right) schemes; fine grid (-*-), medium grid (-○-), coarse grid (-△-), and reference solution (dashed).

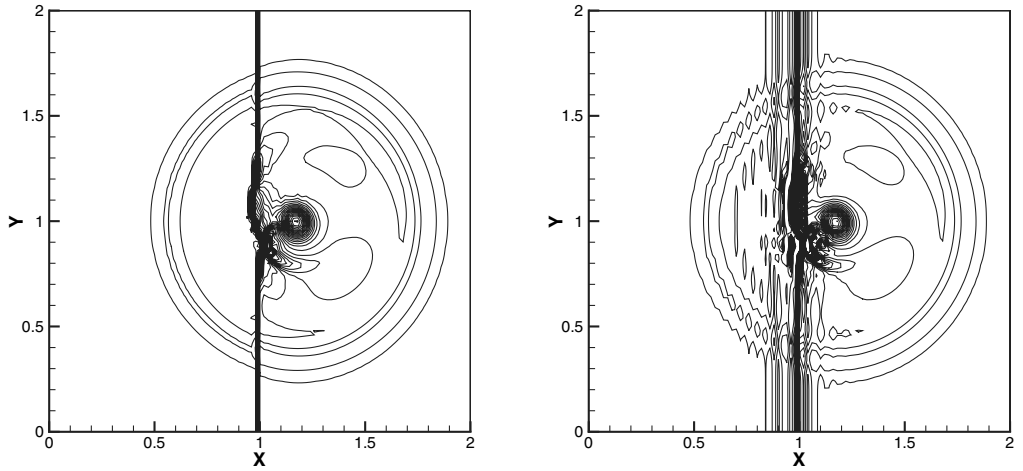

Fig. 13 Pressure contours for the 2-D shock–vortex interaction at $t = 0.72$ and $\Delta t = 4 \cdot 10^{-3}$ (49 contours from 0.527 to 0.845) for the OSMP7 scheme (left) and DRP scheme (right).

The pressure-field contours obtained by using the OSMP7 and DRP schemes are shown in Fig. 13 using 101×101 grid cells. The OSMP7 scheme shows an accurate behavior, without numerical oscillations, whereas the interaction with the shock generates strong oscillations for the DRP scheme.

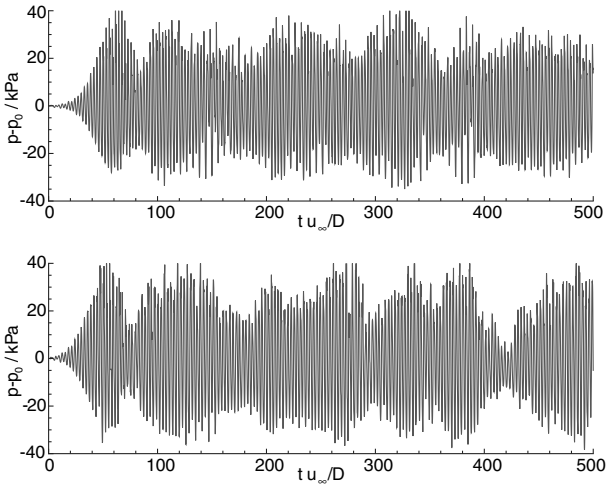

Fig. 14 Time trace of the fluctuating pressure on the cavity floor at (1.16*D*, −1*D*); simulations with OSMP7 (top) and DRP schemes (bottom).

V. Supersonic Laminar Cavity Flow

The last comparison is made in the case of the flow-induced oscillations by a transonic laminar open cavity, which involves moving shocks. A length-to-depth ratio $L/D = 1.5$ and Mach number $M_\infty = 1.5$ configuration with a laminar incoming boundary layer of thickness $\delta = D/5$ was chosen. The computational domain extends $7.5D$ in the streamwise direction and $3D$ in the normal direction. The origin of the axis is located at

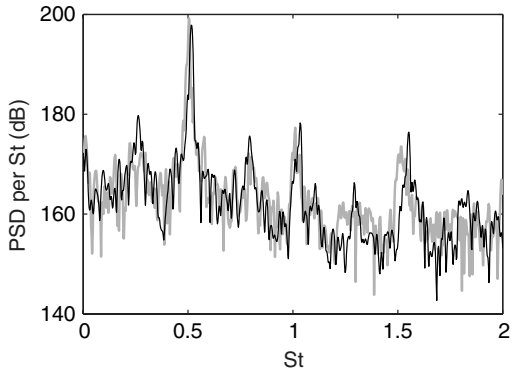

Fig. 15 Power spectral density (PSD) of fluctuating pressure on the cavity floor at (1.16*D*, −1*D*); simulations with OSMP7 (black) and DRP schemes (gray).

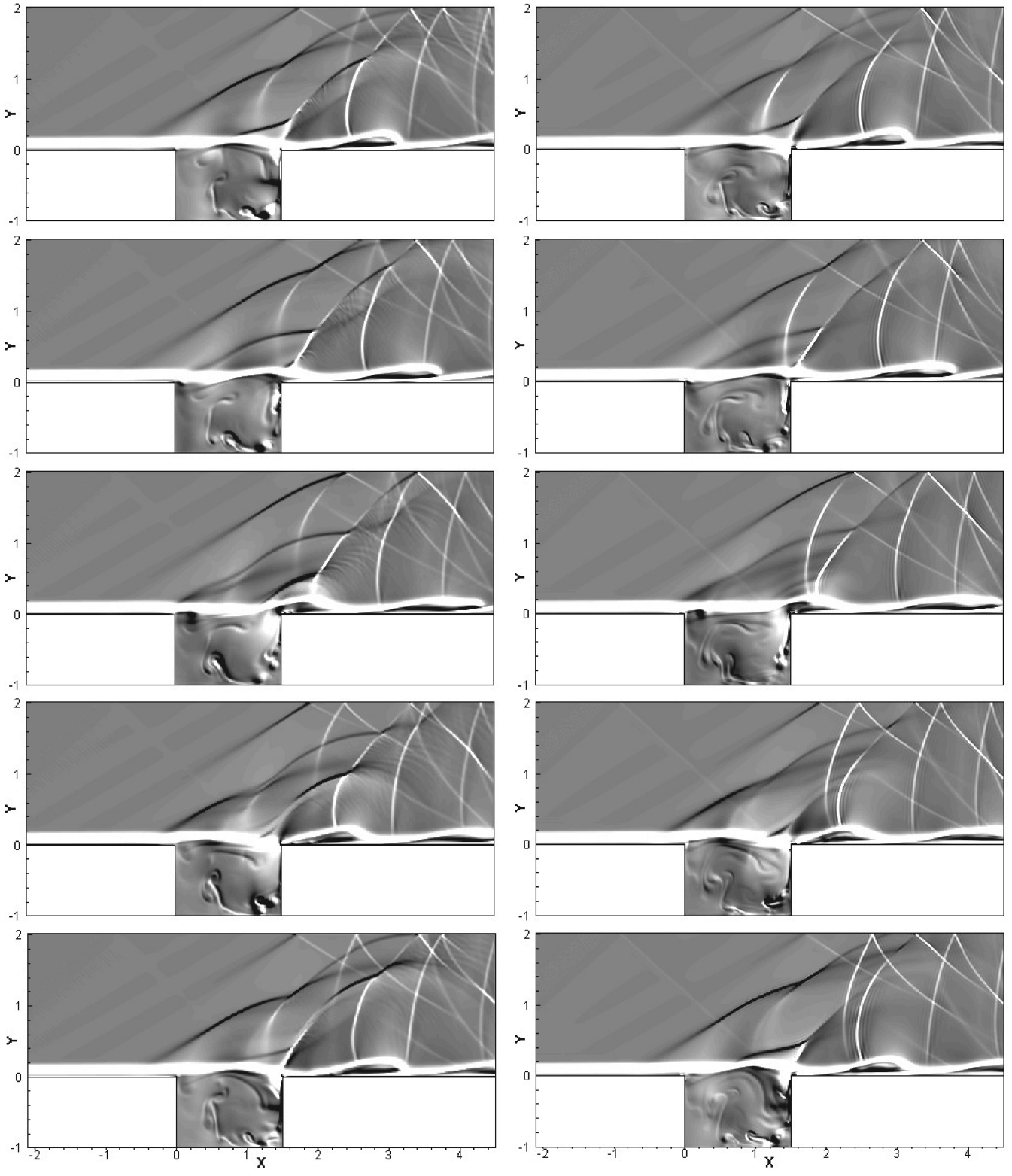

Fig. 16 Cavity flow for five times covering one period $M_\infty = 1.5$; isocontours of $(\partial\rho/\partial x) + (\partial\rho/\partial y)$ (43 levels from -1 to 1); OSMP7 (left) and DRP (right) schemes.

the leading edge of the cavity. At the inlet boundary, the freestream velocity U_∞, Mach number M_∞, static temperature T_∞, and static pressure are, respectively, 514.67 m/s, 1.5, 293 K, and 1.013 hPa. The incoming boundary-layer profile is based on the Crocco–Busemann relations. The molecular viscosity follows Sutherland's law. For air, the freestream Reynolds number is $Re = 1.73 \times 10^4$. We used a uniform 600×240 grid (80 points per length D). The wall boundary conditions are prescribed in the same way as for the supersonic boundary-layer case, using ghost points inside the walls.

After an initial transient, a self-sustained oscillatory state is established. A degree of randomness is, however, superimposed to the periodic oscillatory state, as can be seen in Fig. 14, representing the pressure signal at $(1.16D, -1D)$ obtained with the OSMP7 and DRP schemes. The pressure signals are globally very similar and the amplitudes are comparable. The spectral analysis of the signals in

Fig. 15 indicates the presence of a dominant mode at a Strouhal number $St = fL/U_\infty = 0.51$. Rossiter's formula $St = (n - 0.25)/(1/0.57 + M_\infty)$ gives 0.53 for $n = 2$. This is thus a mode 2 of oscillations.

A schlieren-like visualization is presented in Fig. 16. The isocontours of the quantity $\partial\rho/\partial x + \partial\rho/\partial y$ are depicted for five consecutive times, each time interval corresponding to approximately one-fourth of the period. The results show a regular vortex shedding in the shear layer between the two corners of the cavity. Their impingement upon the downstream corner induces vortical structures swept inside the cavity and forming the principal recirculation zone. When comparing the results obtained using the OSMP7 and DRP schemes, they appear to be very similar, even if some subtle differences can be noticed. They could be attributed to the numerical treatment of the downstream edge of the cavity, which is a singular point. Indeed, we have verified that the flow is very sensitive to the specific implementation of the boundary conditions at this point.

Figure 16 also shows the wave system. The shock-capturing capabilities of the OSMP7 scheme precludes an oscillatory behavior in the vicinity of discontinuities, which can be observed on the DRP results, although the oscillations are weak. The complex wave pattern that develops above the cavity resembles that usually observed in the literature [31–33] and reveals in detail how the main oblique shock waves above the cavity are generated. First, a shock wave is created at the trailing edge, due to the impingement of the vortices shed in the shear layer. This shock wave is steady away from the edge, but close to the shear layer, a lambda-shaped bifurcated shock wave pattern is created to allow the vortex motion. Being "pushed" upward, the left "leg" of the lambda-shaped shock wave propagates upstream. The shock is refracted inside the cavity through the shear layer. When this transmitted wave hits the upstream edge of the cavity, the part inside the cavity reflects on the left wall, and the oblique part above the cavity vanishes, because it can only propagate inside the subsonic part of the boundary layer. At this moment, a new vortex shedding is initiated at the leading edge. In fact, the main shock waves are generated at the downstream edge of the cavity and then propagate toward the upstream edge. No shocks (or only weak shocks) are directly generated at the leading edge, contrary to the commonly admitted view.

VI. Conclusions

A new class of shock-capturing schemes, the OSMPp family, are tested in the area of computational aeroacoustics. The accuracy of the 7th- and 11th-order schemes are analyzed for the advection equation, because space and time discretizations are coupled. The comparison with the DRP scheme of Bogey and Bailly [5] (combining an 11-point-stencil-optimized finite difference scheme, a selective filtering, and a low-dispersion/low-dissipation Runge–Kutta algorithm) indicates that the OSMP11 scheme has a lower dissipation in the low-frequency range and is able to propagate waves with five points per wavelength. The MP condition added to capture discontinuities robustly does not alter high accuracy in the smooth regions.

The behavior of the OSMP schemes for aeroacoustic test problems is in good agreement with the high-order DRP schemes and the reference solutions. The low-dissipation and low-dispersion properties of the OSMP family of schemes is also a feature that can be useful in the large-eddy simulation framework.

References

[1] Lele, S., "Compact Finite Difference Schemes with Spectral-Like Resolution," *Journal of Computational Physics*, Vol. 103, No. 1, 1992, pp. 16–42.

[2] Tam, C., and Webb, J., "Dispersion-Relation-Preserving Finite Difference Schemes for Computational Acoustics," *Journal of Computational Physics*, Vol. 107, No. 2, 1993, pp. 262–281.

[3] Kim, J., and Lee, D., "Optimized Compact Finite Difference Schemes with Maximum Resolution," *AIAA Journal*, Vol. 34, No. 5, 1996, pp. 887–893.

[4] Visbal, M., and Gaitonde, D., "High-Order-Accurate Methods for Complex Unsteady Subsonic Flows," *AIAA Journal*, Vol. 37, No. 10, 1999, pp. 1231–1239.

[5] Bogey, C., and Bailly, C., "A Family of Low Dispersive and Low Dissipative Explicit Schemes for Noise Computation," *Journal of Computational Physics*, Vol. 194, No. 1, 2004, pp. 194–214.

[6] Harten, A., Engquist, B., Osher, S., and Chakravarthy, S., "Uniformly High Order Essentially Nonoscillatory Schemes, 3," *Journal of Computational Physics*, Vol. 71, No. 2, 1987, pp. 231–303; reprint, Vol. 131, No. 1, 1997, pp. 3–47.

[7] Casper, J., and Meadows, K., "Using High-Order Accurate Essentially Nonoscillatory Schemes for Aeroacoustics Applications," *AIAA Journal*, Vol. 34, No. 2, 1996, pp. 244–250.

[8] Adams, N., and Shariff, K., "A High-Resolution Hybrid compact ENO Scheme for Shock-Turbulence Interactions Problems," *Journal of Computational Physics*, Vol. 127, No. 1, 1996, pp. 27–51.

[9] Ekaterinaris, J., "Aeroacoustic Predictions Using High-Order Shock-Capturing Schemes," *International Journal of Aeroacoustics*, Vol. 2, No. 2, 2003, pp. 175–192.

[10] Deng, X., and Zhang, H., "Developing High-Order Weighted Compact Nonlinear Schemes," *Journal of Computational Physics*, Vol. 165, No. 1, 2000, pp. 22–44.

[11] Wang, Z., and Chen, R., "Optimized Weighted Essentially Nonoscillatory Schemes for Linear Waves with Discontinuity," *Journal of Computational Physics*, Vol. 174, No. 1, 2001, pp. 381–404.

[12] Lin, S.-Y., and Chin, Y.-S., "Comparison of Higher Resolution Euler Schemes for Aeroacoustics Computations," *AIAA Journal*, Vol. 33, No. 2, 1995, pp. 237–245.

[13] Nance, D., Viswanathan, K., and Sankar, L., "Low-Dispersion Finite Volume Scheme for Aeroacoustic Applications," *AIAA Journal*, Vol. 35, No. 2, 1997, pp. 255–262.

[14] Chang, S.-C., Wang, X.-Y., and Chow, C.-Y., "The Space-Time Conservation Element and Solution Element: A New High-Resolution and Genuinely Multidimensional Paradigm for Solving Conservation Laws," *Journal of Computational Physics*, Vol. 156, No. 1, 1999, pp. 89–136.

[15] Popescu, M., Shyy, W., and Garbey, M., "Finite Volume Treatment of Dispersion-Relation-Preserving and Optimized Prefactored Compact Schemes for Wave Propagation," *Journal of Computational Physics*, Vol. 210, No. 2, 2005, pp. 705–729.

[16] Schwarzkopff, T., Dumbser, M., and Munz, C.-D., "CAA Using Domain Decomposition and High Order Methods on Structured and Unstructured Meshes," AIAA Paper 2004-2964, 2004.

[17] Titarev, V., and Toro, E., "ADER Schemes for Three-Dimensional Nonlinear Hyperbolic Systems," *Journal of Computational Physics*, Vol. 204, No. 2, 2005, pp. 715–736.

[18] Daru, V., and Tenaud, C., "High Order One-Step Monotonicity-Preserving Schemes for Unsteady Compressible Flow Calculations," *Journal of Computational Physics*, Vol. 193, No. 2, 2004, pp. 563–594.

[19] Harten, A., "High Resolution Schemes for Hyperbolic Conservation Laws," *Journal of Computational Physics*, Vol. 49, No. 3, 1983, pp. 357–393.

[20] Suresh, A., and Huynh, H., "Accurate Monotonicity-Preserving Schemes with Runge–Kutta Time Stepping," *Journal of Computational Physics*, Vol. 136, No. 1, 1997, pp. 83–99.

[21] Tam, C., "Benchmark Problems and Solutions," *ICASE/LaRC Workshop on Benchmark Problems in Computational Aeroacoustics*, CP-3300, NASA Langley Research Center, Hampton, VA, 1995, pp. 1–14.

[22] Tam, C., and Dong, Z., "Radiation and Outflow Boundary Conditions for Direct Computation of Acoustic and Flow Disturbances in a Nonuniform Mean Flow," *Journal of Computational Acoustics*, Vol. 4, No. 2, 1996, pp. 175–201.

[23] Powell, A., "Theory of Vortex Sound," *Journal of the Acoustical Society of America*, Vol. 36, No. 1, 1964, pp. 177–195.

[24] Müller, E.-A., and Obermeier, F., "The Spinning Vortice as a Source of Sound," *Fluid Dynamics of Rotor and Fan Supported Aircraft at Subsonic Speeds*, CP-22, AGARD, Paris, 1967, pp. 22.1–22.8.

[25] Howe, M., "Contributions to the Theory of Aerodynamic Sound, with Application to Excess Noise and the Theory of the Flute," *Journal of Fluid Mechanics*, Vol. 71, No. 4, 1975, pp. 625–673.

[26] Mitchell, B., Lele, S., and Moin, P., "Direct Computation of the Sound from a Compressible Co-Rotating Vortex Pair," *Journal of Fluid Mechanics*, Vol. 285, Feb. 1995, pp. 181–202.

[27] Lee, D., and Koo, O., "Numerical Study of Sound Generation Due to a Spinning Vortex Pair," *AIAA Journal*, Vol. 33, No. 1, 1995, pp. 20–26.

[28] Ekaterinaris, J., "Upwind Scheme for Acoustic Disturbances Generated by Low-Speed Flows," *AIAA Journal*, Vol. 35, No. 9, 1997, pp. 1448–1455.

[29] Bogey, C., Bailly, C., and Juvé, D., "Computation of Flow Noise Using Source Terms in Linearized Euler'S Equations," *AIAA Journal*, Vol. 40, No. 2, 2002, pp. 235–243.
[30] Scully, M., *Computation of Helicopter Rotor Wake Geometry and its Influence on Rotor Harmonic Airloads*, Massachusetts Inst. of Technology, Rept. ARSL TR 178-1, Cambridge, MA, Mar. 1975.
[31] Zhang, X., and Edwards, J., "Analysis of Unsteady Supersonic Cavity Flow Employing an Adaptive Meshing Algorithm," *Computers and Fluids*, Vol. 25, No. 4, 1996, pp. 373–393.
[32] Zhang, X., Rona, A., and Edwards, J., "An Observation of Pressure Waves Around a Shallow Cavity," *Journal of Sound and Vibration*, Vol. 214, No. 4, 1998, pp. 771–778.
[33] Rona, A., and Dieudonné, W., "A Flow-Resonant Model of Transonic Laminar Open Cavity Instability," AIAA Paper 2000-1967, 2000.

D. Gaitonde
Associate Editor